Hybrid Modular Smart Transformer for Asymmetrically Bidirectional Power Flow Operation

Kangan Wang, Youngjong Ko, *Member IEEE*, Rongwu Zhu, *Member IEEE*, Siyu Wu, Weimin Wu, *Member IEEE*, and Marco Liserre, *Fellow IEEE*

***Abstract*—The presence of renewable energy resources in LV distribution networks may lead to a distribution transformer, also known as a Smart Transformer (ST), experiencing the bidirectional power flow. Therefore, the ST must have the capability to operate in both directions. However, the reverse power is less as compared to the forward power, thus the design of ST with the same capacity in both directions increases the hardware cost and decreases the system efficiency. This paper proposes a Hybrid-modular-ST (H-ST), composed of a mixed use of single active bridge-based series resonant converter and dual active bridge instead of complete use of uni- or bi-directional converter adopted in the conventional solid-state-transformer. Based on the proposed H-ST, the impacts of power imbalance among cascaded modules in reverse operation mode are analyzed and then an effective solution based on reactive power compensation combined with the characteristics of the proposed architecture is adopted. The simulation and experimental results clearly validate the effectiveness and feasibility of the theoretical analyses.**

***Index Terms*—Cascaded H-bridge, dual-active bridge, series resonant converter, smart transformer (ST), three-stage architecture.**

I. Introduction

With the continuously increasing penetration of Distributed Energy Resources (DERs) and new sizeable DC loads like Electric Vehicle (EV) charging stations, the modern Low Voltage (LV) distribution grid experiences high voltage violation and overload [1], [2]. A Smart Transformer (ST), which is based on power electronics and integrates communication, as well as advanced control, can provide DC connectivities and potentially reduce the reinforcements caused by DERs and EV charging stations in LV distribution grids [3], [4].

Due to the asynchronous behaviour between the power consumption in loads and generation in DERs, distribution transformers, also the ST, in modern LV distribution grids may suffer from reverse power flow, where the reverse power is generally partial as compared to the forward power flow [5]. Fig. 1(a) shows the phenomenon of the reverse power flow, where the generated power in the LV distribution grid can be more than the consumed power during some periods in one day [6]. Based on such behaviour of power flow, ST will operate in asymmetrical conditions, which provides the realistic possibilities for the cost-efficiency-benefit design of the ST.

Three-stage architecture of ST as shown in Fig. 1(b) can ensure full grid supports and DC connectivities as compared to single- and two-stage ST [7], [8]. Besides, the independent functionalities provided in each stage enable the independent converter design of each stage [9]. Thus, the three-stage ST is considered as one of the most promising ST architectures. Due to the requirement of reactive power support

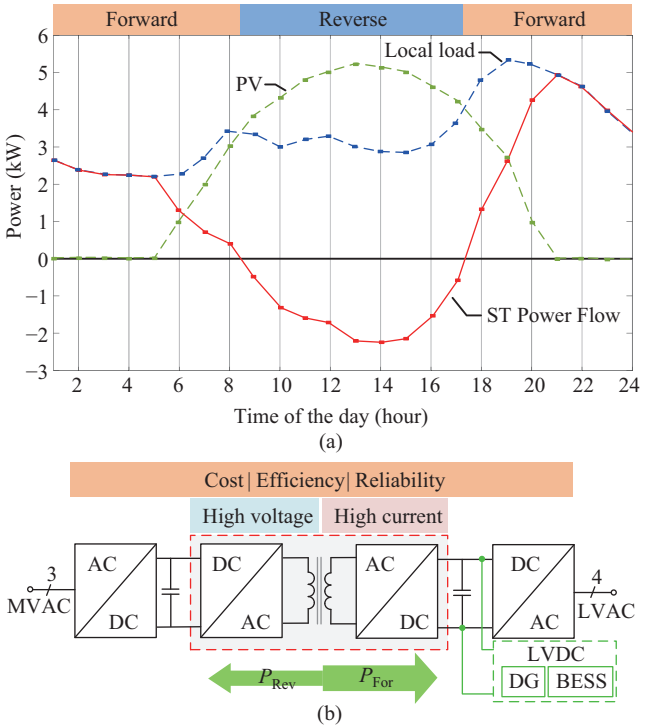

Fig. 1. The power flow and the typical architecture of ST. (a) Profile of load consumption and power generation in distribution grid. (b) Three-stage smart transformer architecture.

Manuscript received August 18, 2022; revised March 27, 2023; accepted May 4, 2023. Date of online publication February 14, 2024; date of current version March 18, 2024. This work was supported in part by National Key Research & Development Project of China (2017YFE0134300), in part by Shanghai 2022 Science and Technology Innovation Action Plan-Star Cultivation (Sailing Program) (22YF1415700) and in part by the National Natural Science Foundation of China under Grant 52307215.

K. A. Wang (corresponding author, email: kawang@shmtu.edu.cn; ORCID: https://orcid.org/0000-0003-3323-0630), S. Y. Wu, and W. M. Wu are with Shanghai Maritime University, Shanghai 201306, China.

Y. J. Ko is with Pukyong National University , Busan 48513, South Korea.

R. W. Zhu is with Harbin Institute of Technology (Shenzhen), Shenzhen 518000, China.

M. Liserre is with Kiel University, Kiel 24118, Germany.

DOI: 10.17775/CSEEJPES.2022.05650

and harmonic compensation in Medium-Voltage (MV) AC grid, the bidirectional MV power converter is needed and in comparison with the two typical industrial solutions of Cascaded-H Bridge (CHB) and Modular Multilevel Converter (MMC), the CHB is a cost-benefit converter for the MV AC/DC stage. The LV DC/AC stage can use commercial two- or three-level inverters [10], which are controlled to construct the LVac grids. In comparison, the DC/DC stage has to meet the strict requirements such as high voltage galvanic isolation, high efficiency and power flow control, which makes the DC/DC stage the most challenging part. The design of DC/DC stage has lots of available choices, such as the uni-directional Single-Active-Bridge (SAB)-based DC/DC converters [11] and the bidirectional Dual-Active Bridge (DAB)-based DC/DC converters [12], [13]. From the point of power flow, DAB-based DC/DC converters have the advantages of satisfying the requirement of bidirectional power flow operation. Reference [14] proposed a hybrid DC transformer (DCT) combining multiple DAB-based Series Resonant Converters (SRCs) and DAB converters with input-series-output-parallel (ISOP) configuration, which can not only achieve bidirectional power flow, but also reduce the power losses by use of high-efficiency reasonant DAB-based DC/DC converters. However, DAB-based converters increase the hardware cost and system complexity, especially in the case that the reverse power is only partial and rarely occurs as compared to the forward power. Compared to the DAB-based DC/DC converters, the SAB-based DC/DC converters does not have the capability of bidirectional power flow, but can offer several advantages. Remarkably, the design efforts and component costs can be significantly reduced by replacing some active semiconductors (e.g. IGBTs and MOSFETs) with diodes. Additionally, required number of auxiliary components such as gate driver units, power suppliers and communication units are reduced. Hence, this solution brings benefits to the system's cost, efficiency and reliability [15]. Based on the above analysis, the flexibility in the DC/DC stage brings the technical conditions for the cost-efficiency-benefit design of the ST. Hence, in this paper, a hybrid DC/DC stage, which mixes the DAB converters and SAB-based SRCs, is proposed to satisfy the design aim, as well as the requirement of asymmetrical-bidirectional power flow operation.

However, unlike the equal power distribution in all modules of the conventional ST architecture, in the proposed Hybrid-modular-ST (H-ST), the forward power flows through both the DAB and SAB-SRC while the reverse power flows through the DAB only. Thus, the operating capability in reverse mode is limited because the CHB cells connected to the SAB-SRC can not provide active power leading to serious imbalance in the CHB converter and thus constraint of modulation index [16]. A few methods are proposed to extend the operation range caused by power imbalance [17]–[20]. A modulation technique of mixing staircase and PWM in the CHB PV systems, where one cell operates in PWM mode while the others are kept in either "charging" or "discharging", is proposed to extend the module power imbalance in [17], [18]. A power equalization method based on the combination of staircase-PWM technique and different zero-sequence injection methods is proposed in [19], which can achieve both module power balance and phase power balance at the same time. Reference [20] proposed an reactive power-based solution to suppress the impacts of unbalanced power generated from PV panels, where the reactive power is redistributed in the cascaded H-bridge cells. Similarly, the above solutions can also be used in the H-ST to extend the system operation range limited by the deactivation of CHB cells connected to unidirectional modules in the reverse condition. However, the reverse operation of H-ST is a special case of power imbalance, where the power imbalance has a strong relationship with the number of unidirectional modules and the active power flowing through unidirectional modules is zero. So, the control method combined with the topology characteristics of H-STs is necessary in further research.

In this paper, the H-ST architecture combining multiple SAB-SRCs and DAB converters is proposed to not only reduce the hardware cost and system complexity, but also can pass the reverse power. Based on the H-ST architecture, the reactive power compensation-based control strategy with consideration of the architecture characteristics is proposed to achieve stable grid-connected operation. The remaining parts of this paper are structured as follows. Section II describes the hybrid modular ST architecture and clarifies the advantages of cost and efficiency. Section III makes analysis of power imbalance in reverse condition and discusses the improved control strategy. Simulation and experimental results are presented to validate the effectiveness of the proposed architecture and control strategy in Sections IV and V. Finally, the conclusion is drawn in Section VI.

II. Hybrid Modular ST Architecture

A. The proposed architecture

The proposed H-ST architecture consists of unidirectional and bidirectional modules and the detailed H-ST architecture is shown in Fig. 2(a), where the detailed circuit schematic diagrams of single unidirectional module and bidirectional module are given in Fig. 2(b) and (c). N_{b} is the number of bidirectional modules and N_{u} is the number of the unidirectional modules. The total number of modules n is equal to $N_{\mathrm{b}} + N_{\mathrm{u}}$.

In the unidirectional module, the SAB-SRC consists of the primary active bridge, the resonant tank, the high-frequency transformer (HFT) and the secondary diode bridge [21]. The most efficient operation point is when it operates in the discontinuous conduction mode (DCM) with the switching frequency (f_{src}) equal or slightly below the resonant frequency (f_{r}) [22], where the primary side switches achieve zero voltage switching (ZVS) and low-current switching while the secondary diodes achieve zero-current switching (ZCS). In the bidirectional module, the DAB converter consists of the input active bridge, the inductor, the HFT and the output active bridge [23]. The active power flows from the active bridge with leading phase angle to the active bridge with lagging phase angle, where the amount of transferred power is controlled by the angle difference between two active bridges.

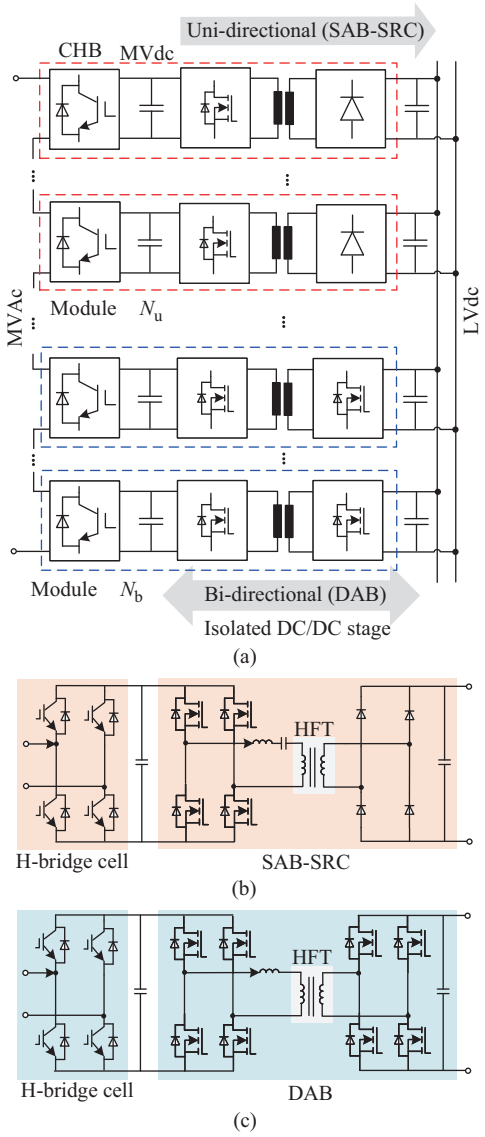

Fig. 2. The proposed H-ST architecture. (a) Proposed H-ST architecture consisting of unidirectional and bidirectional modules. (b) The detailed circuit schematic diagram of single unidirectional module. (c) The detailed circuit schematic diagram of single bidirectional module.

The DAB converter can achieve zero voltage turn-on for all switches [24].

In order to clearly evaluate the performances of the proposed architecture, the standard architecture (CHB+DAB) is considered as a benchmark. For the comparative analysis, both of the two atchitectures must be designed and the key characteristics—cost and power losses must be calculated. Table I gives the basic parameters of the ST architectures, where the capacity of the overall system is 1 MVA and that of each module is 30 kW. The detailed design process of the used converters with consideration of performance optimzation will be illustrated in following parts.

B. Cost and Power Losses Comparisons

1) Cost Comparison

For each module, the total cost is mainly from semiconductors, capacitors, magnetic components, cooling systems and auxiliary components. According to the basic parameters listed in Table I, the H-bridge cell and the used DC/DC converter in each module can be designed and the selected components are summarized in Table II, respectively. Then, the detailed cost models of the proposed and standard ST architectures can be constructed and the cost can be compared.

TABLE I
THE TYPICAL SPECIFICATIONS OF STS

Symbol	Description	Value
V_{g}	Grid Voltage	10 kV
f_{g}	Grid Frequency	50 Hz
S_{g}	Rated System Capacity	1 MVA
P_{H}	H-bridge Cell Capacity	30 kW
n	Cascaded Number	13
V_{MV}	MVdc Voltage	800 V
$P_{\mathrm{dab/src}}$	DC/DC Converter Capacity	30 kW
V_{LV}	LVdc Voltage	800 V

TABLE II
COMPONENTS FOR THE STS

Converters	Components		Details
H-bridge	IGBTs		IKQ75N120CT2XKSA1
	MV capacitors		B36D451LPC651TDA5N
DAB	SiC MOSFETs		C2M0040120D
	HFTs	Core type	E1006028
		Core material	N87
		Wires	Litz
	Inductors	Core type	B66371
		Core material	N87
		Wires	Litz
SRC	SiC MOSFETs		C2M0040120D
	SiC diodes		FFSH40120A
	Resonant capacitors		MKP10
	HFTs	Core type	E1006028
		Core material	N87
		Wires	Litz

The cost of H-bridge cell mainly consists of semiconductors (IGBTs), MVdc capacitors, cooling systems and auxiliary components. Based on the grid voltage and rated system capacity, it can be calculated that the grid current amplitude I_{g} using (A1) listed in Appendix A. According to the MVdc voltage and grid currents, the IGBT IKQ75N120CT2XKSA1 from the big market player is selected for H-bridge cells. Regarding to the MV capacitors, the capacitance should satisfy the constrains to suppress the ripple in the MV DC-links and it can be calculated using (A2), where ω is the ripple angle frequency, V_{MV} is the MVdc voltage and ΔV is the ripple amplitude. Through the calculation, the suitable product is considered to construct the MV capacitor bank. The cooling system also contributes to the cost of H-bridge cells. It is assumed that the cost of the cooling system is proportional to the heatsink volume and only the heatsink volume changes according to the power dissipated in each case. Finally, the cost of cooling system will be proportional to the power dissipation [25]. Combined with the theoretical analysis of power losses in the next subsection and engineering experiences, the cooling modules from Wakefield-vette is used for the H-bridge cells. For the cost evaluation of auxiliary components, the main components are taken into account: gate driver units, auxiliary power supply, communication components, voltage and current sensors, and PCB boards. After the above

parameter design, component selection and cost calculation, the cost model of single H-bridge cell can be obtained.

The cost of DC/DC converters mainly consists of semiconductors (MOSFETs, Diodes), capacitors, maganetic components (HFTs, Inductors), cooling systems and auxiliary components. Based on the basic parameters listed in Table I, the DAB converter is designed with performance optimization, where the MV and LV DC-link voltages are both equal to 800 V. The switching frequency selection is crucial during the dc–dc converter design. Due to that the primary and secondary windings must be spatially separated, the higher switching frequency will result in the obvious proximity effect, which will produce more copper losses. Moreover, given a constant probability of partial discharge, a higher switching frequency will translate into more partial discharge events, with detrimental effects on the transformer lifetime [26]. So 20 kHz is selected as the switching frequency. Considering the reactive power ratio and ZVS range, the inductance is designed as 100μH so that the DAB converter can operate with the optimized shift-phase angle φ= 0.25π [27]. After the design of DAB parameters, the peak value $I_{\mathrm{L(pk)}}$, the RMS values of the HFT currents and the MOSFET currents $I_{\mathrm{L(RMS)}}$, $I_{\mathrm{M(RMS)}}$ can be derived using (A3)–(A5) in Appendix A. According to the results, C2M0040120D is selected as the semiconductors used in DAB converters. The cost of the magnetic components consists of the core cost and the wire cost. Concerning the core cost, the cores from main manufacturers with different geometrical sizes are evaluated according to the feasibility analysis [28]. Then, the parameters of windings are determined based the selected cores. In order to achieve the quantitative assessment of the wire cost, a methodology based on the amount of copper required is adopted, where the number of turns N, the necessary wire area A_{w}, the volume of copper v_{cu}, the weight of copper W_{cu} and the cost of wires C_{cu} are calculated using (A6)–(A10). The cost calculation of cooling system and auxiliary components for DAB converters is similar to that of H-bridge cells.

The cost of SAB-SRCs is modeled through a similar procedure of parameter design, component selection and cost calculation. As mentioned above, the most efficient operating point of the SRC is when it operates with a switching frequency (f_{src}) equal or slightly below the resonant frequency (f_{r}). The related variables are defined as (A11), where ω_{r} is the resonant angular frequency, Z is the characteristic impedance of the resonant network in terms of the resonant inductor L_{r} and capacitors C_{r}, and γ are the frequency ratio. According to the basic parameters listed in Table I, the average value of input port current I_{i}, the output port current I_{o}, the peak values of the resonant capacitor current and the voltage $I_{\mathrm{Lr(pk)}}$, $V_{\mathrm{Cr(pk)}}$, the RMS value of the switch current in the primary side $I_{\mathrm{s(rms)}}$ and the RMS value of the diode current in the seconadry side $I_{\mathrm{d(rms)}}$ can be calculated using (A12)–(A14). Based on the calculated results, C2M0040120D is selected as the switches and FFSH40120A is selected as the diodes in SRCs. About the design of resonant tank, the leakage inductance of the transformer is used to form the resonant circuit for the operating optimization [22] and the corresponding resonant capacitor can be determined. Based on the above analysis, the cost calculation of the SRCs can be implemented following the similar procedure of DAB converters and the cost model can be obtained.

After the construction of cost models of the proposed and standard architectures, the cost characteristics can be compared, which is shown in Fig. 3. Fig. 3(a) shows that the cost of SAB-SRCs is only 65% of that of DAB converters, which means that the use of SRCs can bring the obvious hardware cost reduction in the DC/DC stage. Fig. 3(b) shows the cost of single bidirectional and unidirectional modules. It can be seen that the cost of DC-DC converters accounts for the main part of that of each module, which can reach to 67% in the standard architecture. For the ST architectures, the total cost of the unidirectional module is 76.8% of the bidirectional modules, which means the proposed architecture can bring the obvious hardware cost reduction of the whole system cost.

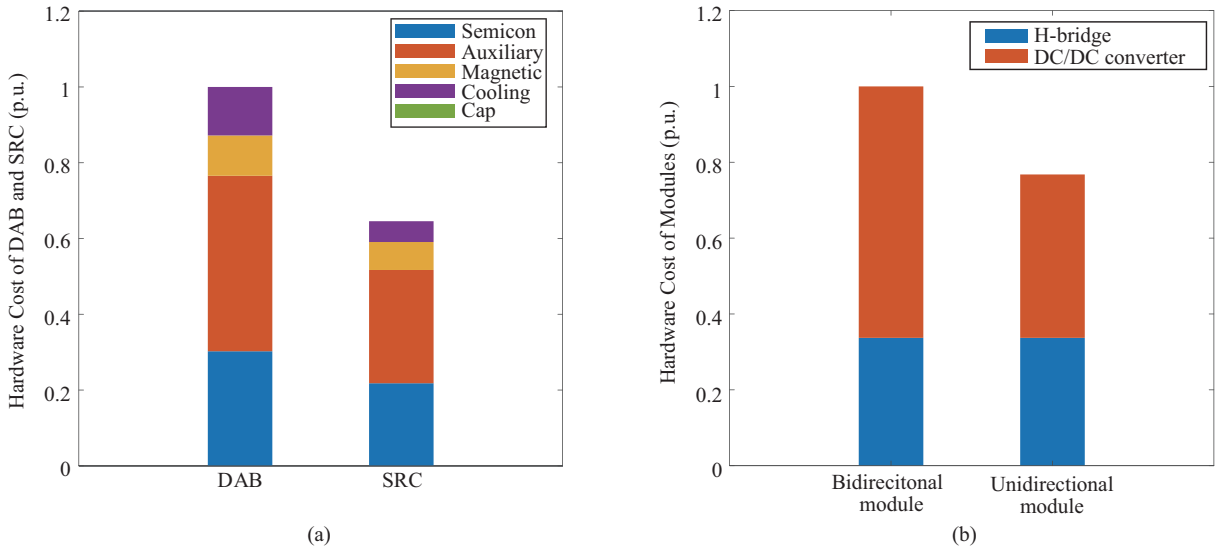

Fig. 3. Cost comparision. (a) Cost of single DAB converter and SAB-SRC. (b) Cost of bidirectional module and unidirectional module.

2) Power Losses Comparison

The power losses are another aspect of the most important performances evaluated in this paper. For each module, the main power losses are from the semiconductors, magnetic components, capacitors.

For the H-bridge cell, the total power losses consist of two parts: (1) IGBT conduction losses, turn-on losses and turn-off losses; (2) diode conduction losses and reverse recovery losses. Based on the electric parameters of the selected devices, the conduction losses of the IGBTs $P_{\mathrm{I\_con}}$ are calculated using (A15), which can be simplified as (A16). The switching losses $P_{\mathrm{I\_sw}}$ can be generally calculated using (A17), where $N_{\mathrm{sw(on))}}$ and $N_{\mathrm{sw(off))}}$ are the number of turn-ON and turn-OFF commutations during the time interval T. The power losses of diodes mainly include conduction losses and reverse recovery losses. The conduction losses of diodes $P_{\mathrm{D\_con}}$ can be calculated using (A18), which can be simplified as (A19) while the reverse recovery losses of diodes $P_{\mathrm{D\_rr}}$ can be calculated using (A20).

For the DC-DC converters, the power losses are related to the operation characteristics of the DAB and SRC. Based on the operation analysis, the total power losses of DAB converters consist of SiC MOSFET conduction losses and the turn-off losses, while the total power losses of SRC consist of SiC MOSFET conduction losses and SiC diode conduction losses. The conduction losses of MOSFETs $P_{\mathrm{M\_con}}$ are calculated using (A21). It can be simplified as (A22), where the ON-resistance R_{ds} is a function of the drain-source current i_{ds}, junction temperature T_{j}, and gate voltage V_{g}. For DAB converters, the turn-ON losses are neglected and a simplified equation of switching losses can be written as presented in (A23). For SRCs, the diode conduction losses can be calculated using (A19). The power losses of the HFTs and inductors mainly include the wire losses P_{wire} and the core losses P_{core}. In the process of design, the Litz wires are used to avoid the skin effect. So only the DC losses on the wires are considered, and it is calculated using (A24). For the core losses, the generalized Steinmetz equation is used, as presented in (A25) and (A26). It can be further simplified as (A27), which approximates the core losses dependent on the switching frequency f_{dc}, the peak value of the magnetic flux density B_{pk} and the core volume V_{core} for a given core. K_{stm}, a_{stm} and b_{stm} are the coefficients which are dependent on the core material. The power losses of capacitors mainly include the dielectric losses and heating losses. In the MV H-birdge cell, the metalized electrolytic-type capacitors are used while the film-type capacitors are used in the DC/DC stage. Combined with system operation and component selection, the dielectric losses P_{d} and the heating losses P_{th} can be obtained using (A28) and (A29), respectively.

Based on the above calculations, the power losses of each module in the proposed and standard architectures can be compared. The relative power losses of power module can be obtained, which is shown in Fig. 4. It can be seen that the power losses of single unidirectional module is only 78.6% of single bidirectional module in the rated condition. In order to show the efficiency characteristics of the unidirectional and bidirectional modules, the efficiency curves with different operating power are depicted in Fig. 5. It can be seen that the efficiency of the unidirectional module is always higher than that of the bidirectional module. Especially in the condition with very low or high module power, the efficiency difference become larger, which means the proposed architecture can bring the better efficiency performance of STs in the whole operation period.

In order to further show the characteristics of the proposed architecture, the extended comparisons among CHB+DAB, the proposed and the CHB+AB-DC/DC for asymmetrical power flow in [29] are shown in Table III, where the comparisons qualitatively evaluate hardware cost, efficiency, control complexity, component number, power transfer capability. Compared with CHB+DAB converters, the CHB+AB-DC/DC converter shows a certain advantage on hardware cost by replacing

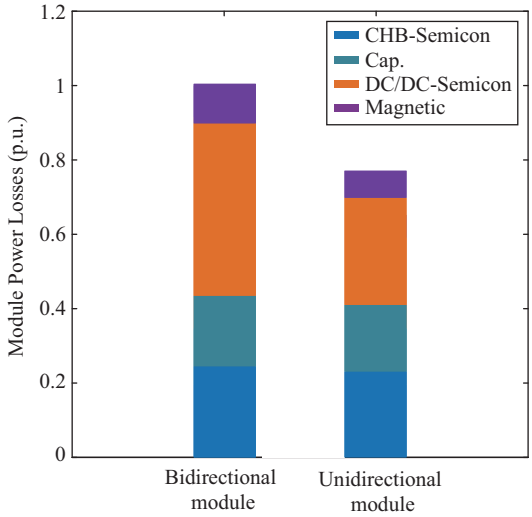

Fig. 4. Power loss comparison of the bidirectional module and the unidirectional module with rated module power.

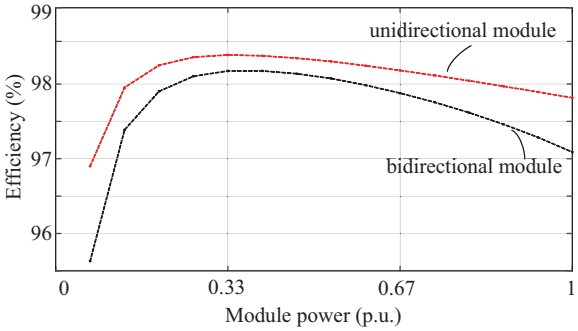

Fig. 5. Efficiency comparison of the unidirectional module and the bidirectional module with varied module power.

TABLE III
EXTENDED COMPARISONS OF ST ARCHITECTURES FOR ASYMMETRICALLY BIDIRECTIONAL POWER FLOW OPERATION

Item	CHB+DAB	CHB+AB-DC/DC	Proposed
Hardware cost	+++	++	+
Efficiency	++	++	+++
Control complexity	+	++	++
Component Number	++	+++	++
Power capability	+++	++	++

the expensive high-power-rating SiC Mosfets with available diodes, but average performance in terms of efficiency while the proposed architecture shows better performances on hardware cost and efficiency due to the use of unidirectional power modules. The CHB+AB-DC/DC converter and the proposed one have two operation modes with respect to the power flow direction, which result in the control system has a slightly higher control complexity. Besides, the power transmission capability in the reverse condition is dependent on the system requirement, which needs be considered in the design process.

III. Power Imbalance and Control Strategy of the Proposed Architecture

A. Power imbalance in reverse condition

In the reverse condition, if the unidirectional modules deactivate and the system keeps operation with unit power factor, the simplified diagram of power flow is shown in Fig. 6(a), where the DC-link voltages of all H-bridges are controlled to be equal to V_{MV} and the AC voltages of the H-bridges can be obtained as:

$$\vec{v}_x = \vec{m}_x V_{\mathrm{MV}} \tag{1}$$

where subscript "x" represents the x^{th} H-bridge module and $\vec{m}$ is the module modulation vector.

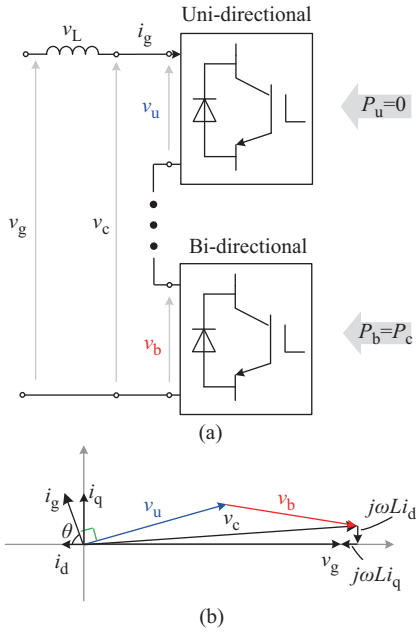

Fig. 6. Power imbalance and the control strategy based on reactive power compensation combining with the characteristics of H-STs in the reverse condition: (a) The power flow in reverse condition. (b) The phasor diagram with the reactive power control strategy.

Since the H-bridges are connected in series to synthesize the total AC voltage, based on (1), the total AC voltage $\vec{v}_{\mathrm{c}}$ can be expressed as:

$$\vec{v}_{\mathrm{c}} = \sum_{x=1}^{N_{\mathrm{u}}+N_{\mathrm{b}}} \vec{v}_x = V_{\mathrm{MV}} \sum_{x=1}^{N_{\mathrm{u}}+N_{\mathrm{b}}} \vec{m}_x \tag{2}$$

where $\vec{v}_{\mathrm{c}}$ presents the AC voltage vector of the CHB converter, N_{u} and N_{b} are the number of unidirectional and bidirectional modules, respectively.

It clearly shows that in (2) the output voltage range is determined by the sum of modulation vectors. Furthermore, due to the series connection of H-bridge modules, the AC current in each H-bridge is identical and the active power can be calculated as (3).

$$P_{\mathrm{c}} = \frac{1}{2}|\vec{v}_{\mathrm{c}}||\vec{i}_{\mathrm{g}}| = \frac{V_{\mathrm{MV}}}{2}|\vec{i}_{\mathrm{g}}| \sum_{x=1}^{N_{\mathrm{u}}+N_{\mathrm{b}}} |\vec{m}_x| \tag{3}$$

where $\vec{i}_{\mathrm{g}}$ is the AC current vector.

Similarly, (3) shows that the power flowing through each H-bridge cell is determined by the module modulation vector. In reverse operation with the unit power factor, since the unidirectional modules can not deal with active power, the reverse power only flows through the bidirectional modules and the modulation indexes of the unidirectional modules are nearly equal to 0 [30]. Thus P_{c} can be expressed as (4).

$$P_{\mathrm{c}} = \frac{1}{2}|\vec{v}_{\mathrm{c}}||\vec{i}_{\mathrm{g}}| = \frac{V_{\mathrm{MV}}}{2}|\vec{i}_{\mathrm{g}}| \left(\sum_{x=1}^{N_{\mathrm{b}}} |\vec{m}_x| + \sum_{x=N_{\mathrm{b}}+1}^{N_{\mathrm{b}}+N_{\mathrm{u}}} 0 \right) \tag{4}$$

The synthesized voltage vector will be equal to (5).

$$\vec{v}_{\mathrm{c}} = V_{\mathrm{MV}} \sum_{x=1}^{N_{\mathrm{b}}} \vec{m}_x \tag{5}$$

In case of grid-connected operation, the reduction of operational modules (from $N_{\mathrm{u}} + N_{\mathrm{b}}$ to N_{b}) would lead to either increasing modulation index or increasing DC-link voltage. However, increasing DC-link voltage implies oversized design in power semiconductors, DC-link capacitors and transformers, potentially impacting the soft-switching behavior and efficiency. Consequently, the modulation index needs to be changed.

Assuming the nominal system modulation index is M_{s} and considering the constraint of the maximum index not larger than 1.0, the relationship among the maximum number of the unidirectional module $N_{\mathrm{u\_max}}$, the number of bidirectional module N_{b}, and nominal modulation index M_{s} can be obtained as:

$$N_{\mathrm{b}} = [M_{\mathrm{s}}(N_{\mathrm{u\_max}} + N_{\mathrm{b}})]. \tag{6}$$

This relationship is visualized shown in Fig. 7(a), considering different nominal modulation index M_{s}, 0.7 (red), 0.8 (blue) and 0.9 (black). Here, the vertical axis represents the number of unidirectional modules with different total numbers of the mixed module from 2 to 20 in the horizontal axis. As it is seen, the lower modulation index and the larger number of total modules allow the larger number of unidirectional modules. The relation is generalized in Fig. 7(b), as representing the number of unidirectional modules per-unit in the system level. Consequently, it is clearly shown that the modulation index limits the number of unidirectional modules. In case of 0.7, the maximum is limited to 30% of the number of total modules, whereas it is 20% and 10% with 0.8 and 0.9 modulation index, respectively.

Above all, although the larger proportion of unidirectional modules is more advantageous to cost and efficiency, the maximum proportion of unidirectional modules is limited by grid-connected operation.

B. Control Strategy for H-STs

The traditional control system of the standard smart transformers is mainly composed of two parts [31]: the control of the cascaded modular ac-dc converter (CHB converter) and the control of the bidirectional isolated DC-DC converters (DAB converters), where the cascaded modular ac-dc converter achieves the grid-connected active and reactive power control and the DC-link voltage balance of cascaded H-bridge cells, while the bidirectional isolated DC-DC converters achieve the control of DC bus voltage. However, if adopting the above control system for the proposed ST architecture, it will meet two challenges: 1) due to the different characteristics of unidirectional and bidirectional modules, in the forward condition the power flowing among the modules is not balanced; 2) due to the inaction of unidirectional modules in reverse condition, the grid-connected operation can not be ensured, which is as discussed in Section III-A. For the above challenges, combining with the characteristics of the proposed architecture, this paper proposes the intercross control structure-based reactive power compensation control strategy to ensure the balanced power distribution among modules and further improve the proportion of unidirectional modules.

1) Control Strategy

The schematic diagram of the proposed control strategy is illustrated in Fig. 6(b), where H-STs makes full use of the

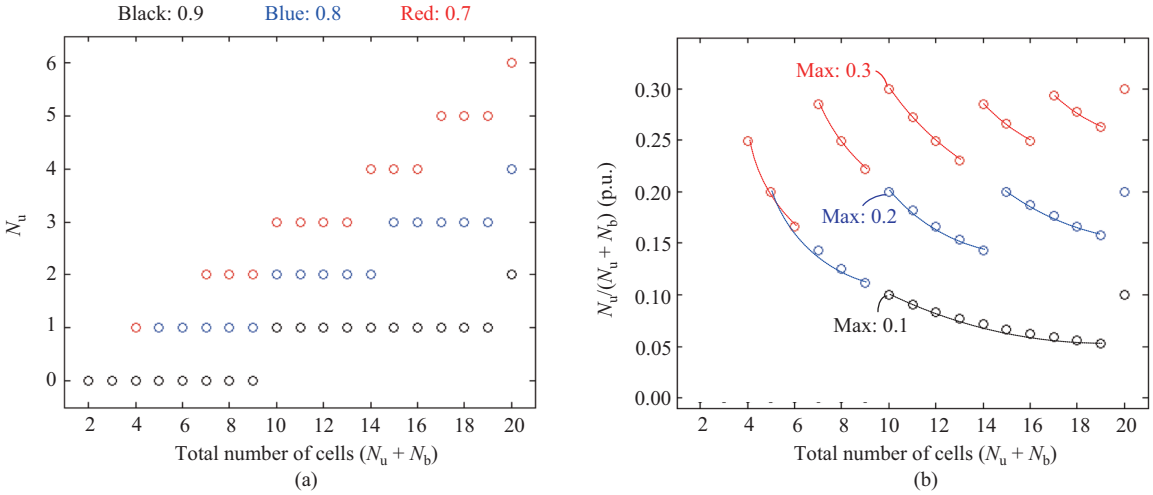

Fig. 7. The relationship between the number of undirectional modules and that of the total modules. (a) Analysis for the number of unidirectional modules available as a function of nominal modulation index and (b) its representation in per-unit in the system level.

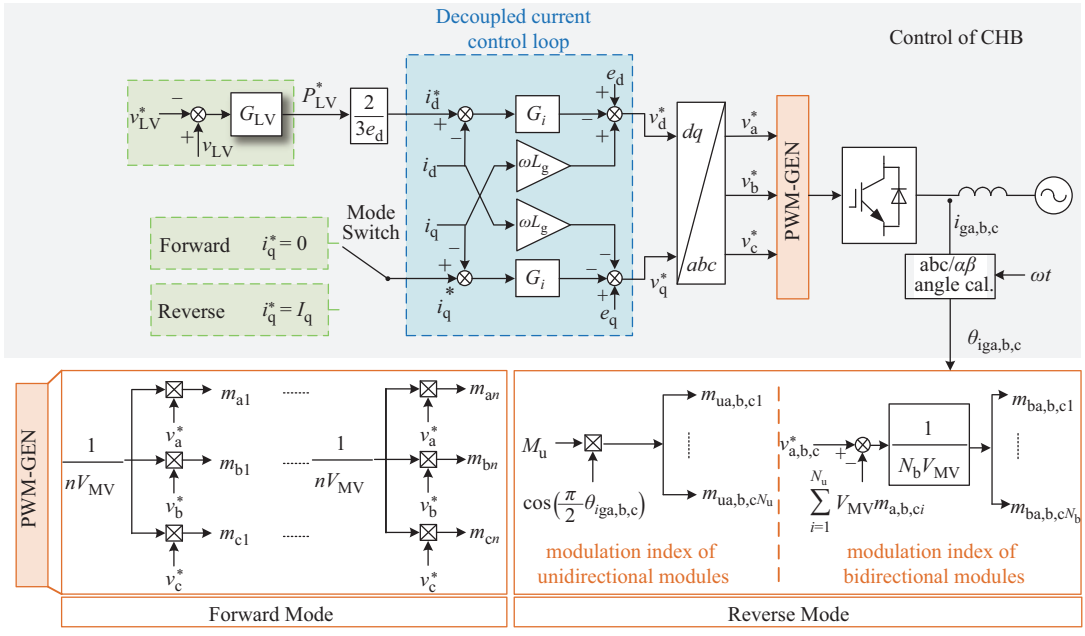

Fig. 8. The control block diagram for the proposed ST architecture in the forward and reverse condition.

unidirectional modules to transfer the reactive power instead of inaction in reverse mode. Thus, the voltage of unidirectional modules $\vec{v}_{\rm u}$ must be always orthogonal against the grid current $\vec{i}_{\rm g}$, but that of bidirectional modules $\vec{v}_{\rm b}$ has flexibility in amplitude and phase control.

The detailed control block diagram for proposed ST is depicted in Fig. 8. The traditional voltage loop of the cascaded modular DC-AC converter controls the H-bridge DC-link voltage, $v_{\rm MV}$, while in this paper the cascaded modular DC-AC converter controls the LV DC bus voltage, $v_{\rm LV}$. The H-bridge DC-link voltage, $v_{\rm MV}$, is controlled by the isolated DC-DC converters. In the modulation stage, in forward mode the modulation waveforms for all modules in one phase are identical, and the modulation waveforms for different phases are with the same amplitude and the shift-phase angle of $\frac{2\pi}{3}$; In reverse mode, the modulation waveforms for unidirectional modules are with amplitude $M_{\rm u}$ and phase angle $(\frac{\pi}{2}-\theta_{i{\rm ga,b,c}})$ while that for bidirectional modules are produced by the difference between the referring phase output voltage and the output voltage of the unidirectional modules.

2) Operation Range

In the following analysis to derive the available operation range based on the proposed reactive power strategy, it is assumed that the rated reverse active power is 0.3 [p.u.] with respect to the rated forward active power and the filter inductance is 1 mH.

The maximum amplitude of reactive current $|\vec{i}_{\rm q,max}|$ can be found as a function of the amplitude of reverse active current $|\vec{i}_{\rm d}|$ as described in (7).

$$|\vec{i}_{\rm q,max}| = \sqrt{I^2 - |\vec{i}_{\rm d}|^2} \tag{7}$$

where I is the amplitude of rated grid-connected currents.

The active and reactive components of inverter voltage $\vec{v}_{\rm c}$ are found by (8).

$$\begin{cases} |\vec{v}_{\rm c,d}| = |\vec{v}_{\rm g}| - |\vec{v}_{\rm L}|\sin(\theta) \\ |\vec{v}_{\rm c,q}| = |\vec{v}_{\rm g}|\cos(\theta) \end{cases} \tag{8}$$

where $\vec{v}_{\rm L}$ is the voltage drop across the filter inductor and θ is the current phase angle, which is obtained by $\cos^{-1}(|\vec{i}_{\rm d}|/|\vec{i}_{\rm g}|)$.

The d- and q-axis components of $\vec{v}_{\rm u}$ are found by as:

$$\begin{cases} |\vec{v}_{\rm u,d}| = |\vec{v}_{\rm u}|\sin(\theta) \\ |\vec{v}_{\rm u,q}| = |\vec{v}_{\rm u}|\cos(\theta) \end{cases} \tag{9}$$

By subtracting the unidirectional modules' voltage $\vec{v}_{\rm u}$ from the inverter voltage $\vec{v}_{\rm c}$, the active and reactive voltage of bidirectional modules is found as (10).

$$\begin{cases} \vec{v}_{\rm b,d} = \vec{v}_{\rm c,d} - \vec{v}_{\rm u,d} \\ \vec{v}_{\rm b,q} = \vec{v}_{\rm c,q} - \vec{v}_{\rm u,q} \end{cases} \tag{10}$$

Finally, the voltage of bidirectional modules $v_{\rm b}$ is derived by (11).

$$\vec{v}_{\rm b} = \vec{v}_{\rm b,q} + \vec{v}_{\rm b,d} \tag{11}$$

Based on the above equations, the capability of the reactive power operation is analyzed under different number of unidirectional modules, considering the system consists of total 13 modules. First, the results with 2 of $N_{\rm u}$ (15.38% of 13) are shown in Fig. 9, where the amplitude and phase of $v_{\rm b}$ are presented in (a) and (b), respectively. The amplitude of $v_{\rm u}$ is fixed to have 0.8 modulation index and it is orthogonal against the grid current. Over the whole reverse active power (0.1–0.3 p.u.), the amplitude and phase of $v_{\rm b}$ are decreasing as increasing the reactive power as shown in Fig. 9(a) and (b), respectively. The power factor is shown in Fig. 9(c), where the full operating region is available when the active power is 0.1 [p.u.], i.e. the reactive power can be controlled between 0 to 1 [p.u.], whereas the 0.3 [p.u.] active power limits the reactive power up to 0.95 [p.u.].

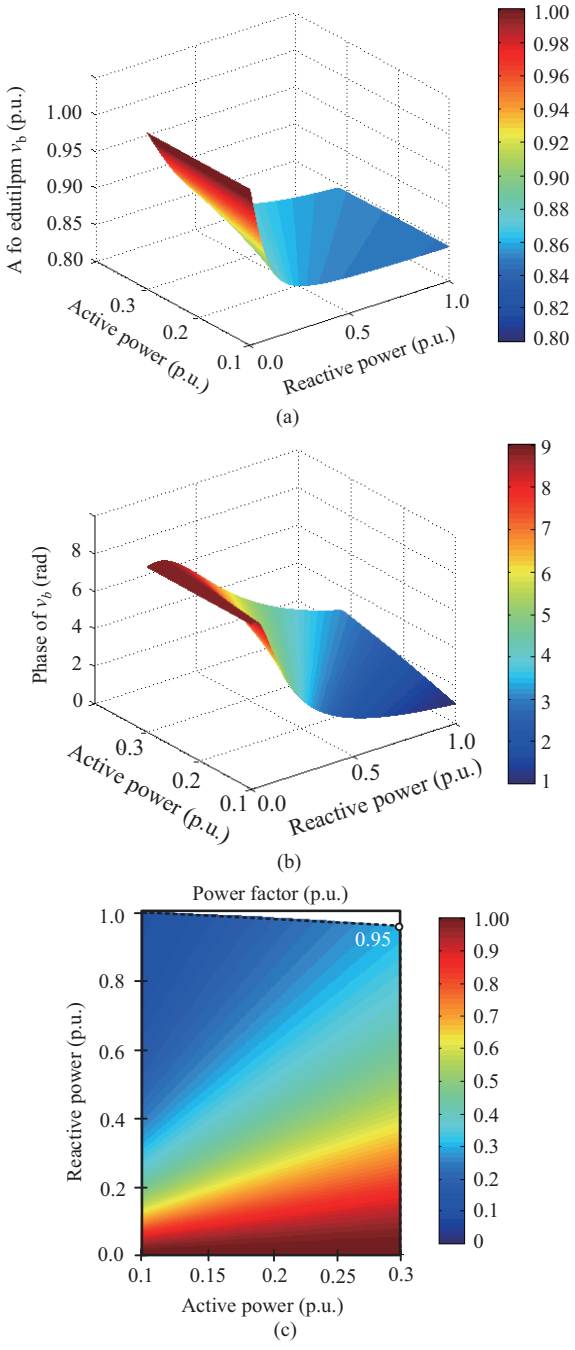

Fig. 9. Available operating condition when $N_{\rm u} = 2$ and $N_{\rm b} = 11$. (a) Amplitude. (b) Phase of $v_{\rm b}$. (c) Power factor.

The available operating region is presented in Fig. 10, under different system design N_{u} and N_{b}. Here, the total number of modules is fixed at 13. Compared to Fig. 9(c), the operating region is limited from 0.07 to 1 [p.u.] with the 0.1 [p.u.] reverse power, and for the 0.3 [p.u.] reverse power the reactive power from 0.2 to 0.95 [p.u.] is allowed in case of Fig. 10(a). As it can be noticed in Fig. 10(b) and (c), as increasing the number of unidirectional modules N_{u}, the available operating region is further restricted. Namely, higher reactive power is necessary for a same reverse active power with the increased N_{u}.

As shown in the previous analysis, the increased number of unidirectional modules restricts the system operation region with the increased required reactive power compensation. In order to extend the operation region, the amplitude of v_{u} is also a candidate to be adjusted (i.e. the modulation index of unidirectional modules M_{u}). The influence of M_{u} on the required minimum reactive power is explored in Fig. 11. Seeing the case with $M_{\mathrm{u}} = 0.8$, the required reactive power is identical with that in Fig. 10. As increasing the modulation index, the required reactive power is decreased, which means that the operation region is extended. For all cases, increasing

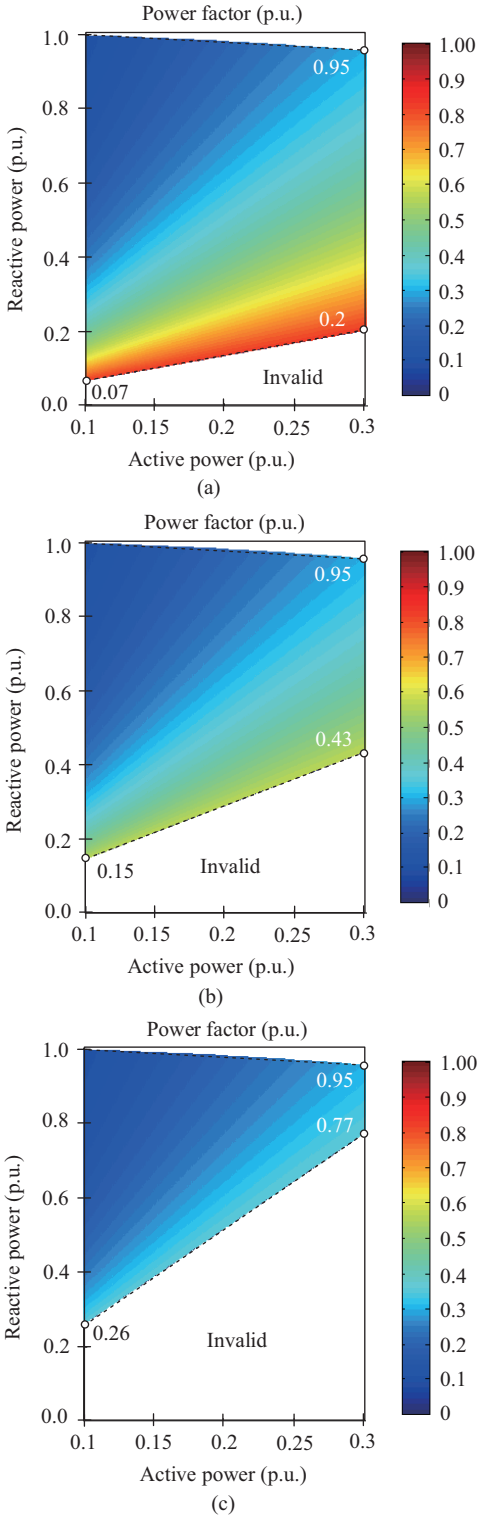

Fig. 10. Available operating region with different numbers of SAB-SRC and DAB when (a) $N_{\mathrm{u}} = 4$ and $N_{\mathrm{b}} = 9$. (b) $N_{\mathrm{u}} = 6$ and $N_{\mathrm{b}} = 7$ and (c) $N_{\mathrm{u}} = 8$ and $N_{\mathrm{b}} = 5$.

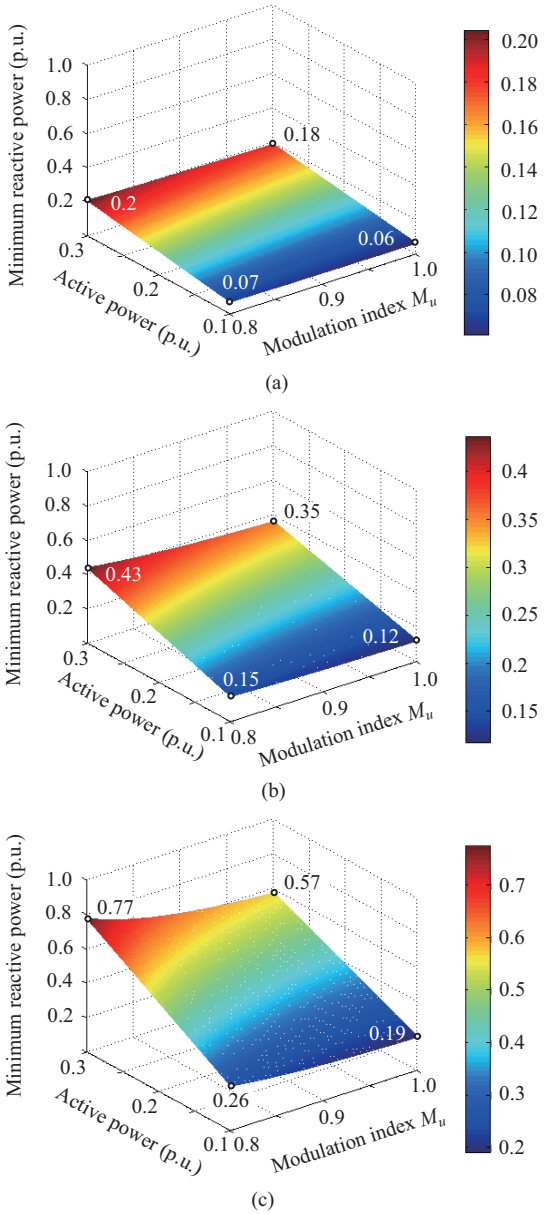

Fig. 11. Minimum reactive power depending on M_u when (a) $N_u = 4$ and $N_b = 9$. (b) $N_u = 6$ and $N_b = 7$ and (c) $N_u = 8$ and $N_b = 5$.

modulation index allows an extended operation region. The maximum effect is shown in case of Fig. 11(c) when the reverse power is 0.3 [p.u.]. The operation region is extended by 0.2 [p.u.] (from 0.77 to 0.57) with the maximum modulation index ($M_{\mathrm{u}} = 1$).

Based on the above analysis, the proposed control strategy can extend the operation range in reverse condition and improve the proportion of unidirectional modules, which offers a possibility to have better device performances compared to the system with traditional control strategy.

C. System Design for H-STs

Considering the performance of DC-DC stage, the system power transmission requirements and the control strategy, the detailed flowchart for cost-efficicency-benefit design of H-STs is shown as Fig. 12. According to given system parameters and the available power switches, the MV side DC-link voltage V_{MV} and the number of modules n are set. Due to the fact that the H-ST has to meet the power transmission requirements in reverse condition, the number of bidirectional power modules can not be smaller than $[nP_{\mathrm{u}}/S_{\mathrm{g}}]$, where $[x]$ is an integer not less than x. Considering the better performance, the number of bidirectional power modules is taken as $[nP_{\mathrm{u}}/S_{\mathrm{g}}]$ and the number of unidirectional power modules is $n - [nP_{\mathrm{u}}/S_{\mathrm{g}}]$. Based on the unidirectional and bidirectional module numbers, the power imbalances in reverse condition are analyzed and the required reactive power is checked whether it can be met according to Section III-B. If it meets the basic requirements, the power module design can be carried out based on cost and efficiency models in Section II-B. Finally, the optimized design scheme aiming at achieving best cost-efficiency-benefit H-STs is selected.

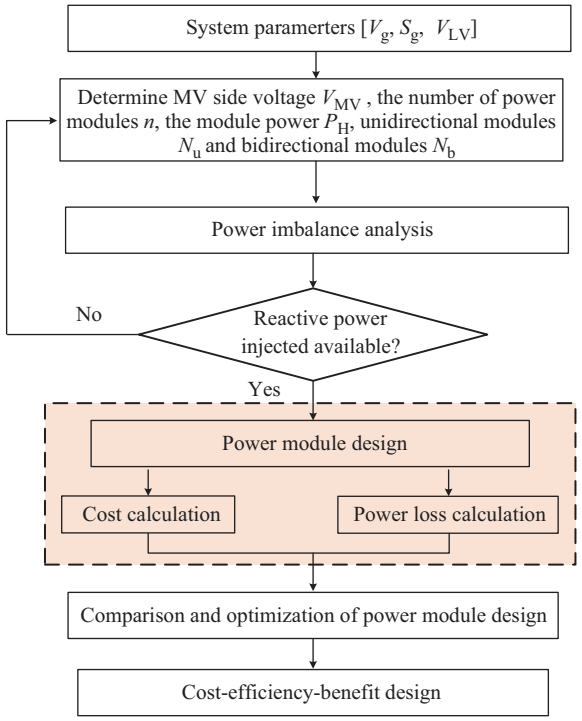

Fig. 12. The detailed design flowchart.

IV. Simulation Validation

To verify the proposed topology architecture and reactive power compensation method, a single-phase ST with 13 H-bridge cells was modeled in Matlab/Plecs, where the specifications are consistent with Table I. In this system, the rated power of each DC/DC module is 10 kW and thus the system rated power is 130 kW. The number of CHB cells fed by SAB-SRC is 4 and by DAB is 9. The loads and DERs in the LV side are simplified as a controllable power source to produce the forward and reverse power flow.

Figure 13 shows the simulation results of the proposed hybrid modular ST. In Stage 1, ST works in the forward operation mode and the total active power consumed at the LV side P_{c} is 130 kW as shown in Fig. 13(a). The 130 kW power is equally distributed in 13 DC/DC converters. The normalized grid current i_{g}^{*} and the current references in d- and q-axis $i_{\mathrm{gd,ref}}$, $i_{\mathrm{gq,ref}}$ are also shown in Fig. 13(b), where the reactive current component i_{gq} is controlled to be 0 A and the grid current only includes active component with the amplitude of 31.5 A. In this stage, the grid current and the modulation waveforms of bi- and unidirectional power modules have a similar phase as shown in Fig. 13(c1). In order to clearly show the amplitude and phase relationship between the grid current and output voltages of CHB cells, the phasor diagrams of the normalized grid current and modulation waveforms of uni- and bi-directional CHB cells are shown in Fig. 14(a), where it can be seen that the phase difference between the normalized grid current and the modulation waveforms of CHB cell is near 0. The modulation waveforms for the uni and bidirectional CHB cells are identical in the forward power flow condition. The output voltage of the CHB converter v_{c} are shown in Fig. 13(c3), where it can be seen output voltage is 27-level. The LV bus voltage is controlled to 800 V by the CHB converter while the DC-lnik voltage of CHB cells are regulated to 800 V by the DC/DC converter as shown in Fig. 13(d) and (e). Besides, the average port currents of single DAB and SAB-SRC in the MV and LV sides are identical as shown in Fig. 13(e), which means transferred power of each DC/DC converter is equal.

At the Stage 2, the consumption active power P_{c} in the LV side continuously decreases until to 0 kW, as shown in Fig. 13(a), and the d-axis component of gird current reference $i_{\mathrm{gd,ref}}$ has similar behaviour as shown in Fig. 13(b). Due to the dynamic response of the voltage control loop in CHB, the LV bus voltage increases slightly during the dynamic period as shown in Fig. 13(d). Until the consumption active power decreases to 0 kW, the reverse power increases from 0 kW until to 39 kW (0.3 p.u), which is in the reverse operation as shown in Fig. 13(a). According to the analysis in Section II and IV, the unidirectional DC/DC converters will be deactivated. The active power is only processed through the bidirectional modules and the unidirectional modules only inject reactive power. $i_{\mathrm{gq}} = -9$ A reactive current is injected into the grid at $P_{\mathrm{c}} = 0$ kW as shown in Fig. 13(b).

In the reverse mode, the modulation waveforms of the CHB cells need to be redistributed. Through the angle calculation module on the grid current, the phase of the grid current is

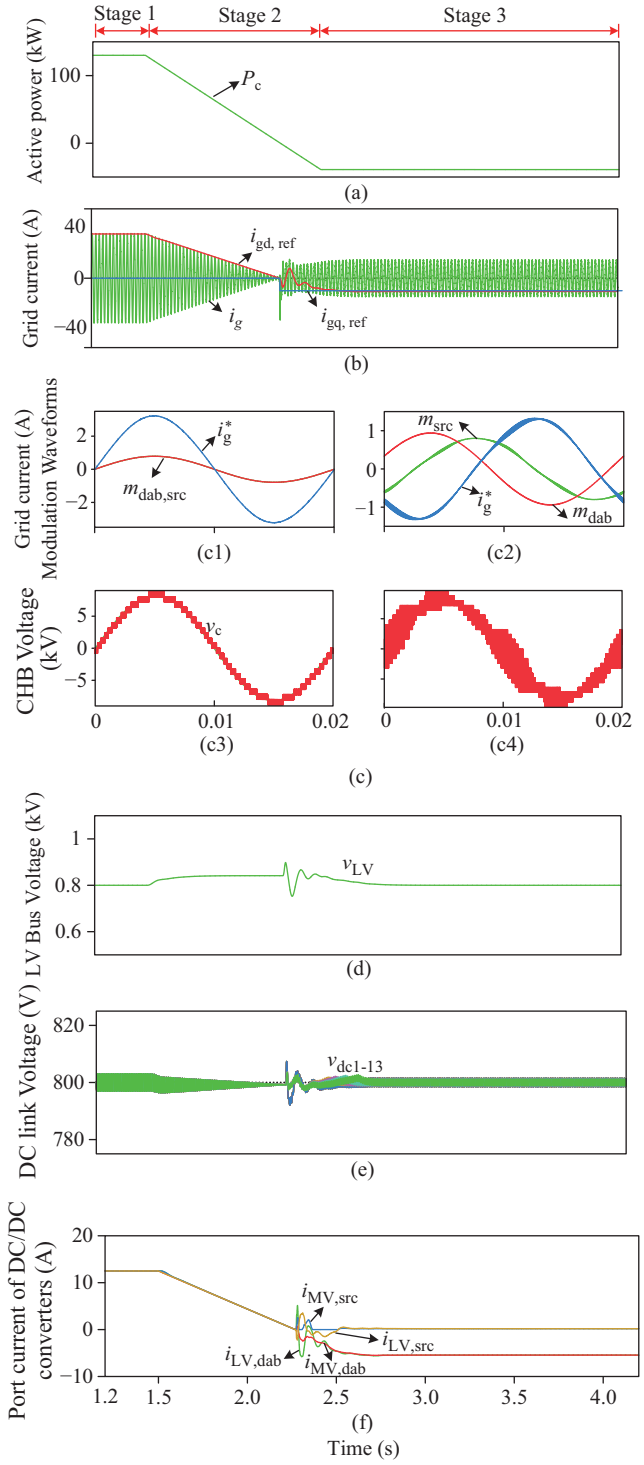

Fig. 13. Simulation results of the single-phase ST with 13 cascaded H-bridge modules. (a) The total active power in the LV side. (b) The gird current and the current references. (c1) The grid current and modulation waveforms in forward mode. (c2) The grid current and modulation waveforms in reverse mode. (c3) The CHB output voltage in forward mode. (c4) The CHB output voltage in reverse mode. (d) The LV Bus voltage. (e) The DC-link voltages of H-bridge cells. (f) The MV and LV side port currents of DAB and SAB-SRC.

obtained. Based on the obtained grid current phase, the uni-directional CHB cells produce the orthogonal output voltages with $M_u = 0.8$ against the grid current. The bidirectional CHB cells are modulated to ensure the converter output voltage equal to the reference output voltage produced by the CHB control loops, which can be seen in Fig. 13(c2). Due to the different amplitudes and phases of the uni- and bi-directional CHB cells, it can be seen converter output voltage v_c has more steps (Fig. 13(c4)). With the control of LV bus voltages in CHB converter and the control of DC-link voltages in DC/DC converters, the LV bus voltage and the DC-link voltages can be regulated back to the reference values after the dynamic period as shown in Fig. 13(d) and Fig. 13(e). Besides, the average port currents of single DAB and SAB-SRC in the MV and LV sides are not equal as shown in Fig. 13(f), where the port currents of signal SAB-SRC are 0 A while 5.4 A in the DAB converters.

The phasor diagrams of the normalized grid current and modulation waveforms of uni- and bi-directional CHB cells in the reverse power flow condition are shown in Fig. 14(b), where it can be seen that the normalized grid current phasor is orthogonal against the modulation waveform phasor of the unidirectional CHB cells. The modulation waveforms for the uni- and bi-directional modules have different amplitudes and phases.

V. Experimental Results

A single-phase seven-level CHB experimental prototype has been built and tested to verify the effect of reactive power compensation and optimized distribution in the reverse mode. The picture of the experimental prototype is shown in Fig. 15 and the experimental procedure is explained in Fig. 16.

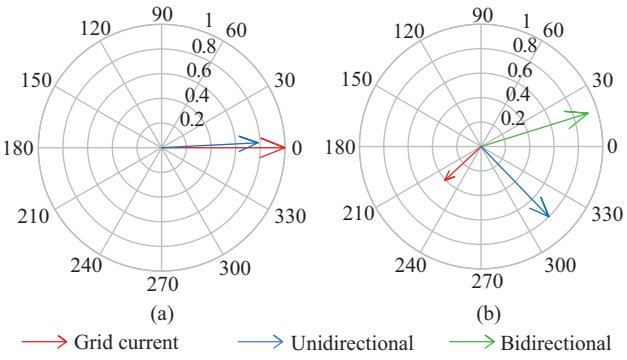

Fig. 14. The phasor diagrams of the normalized grid current and modulation waveforms of H-bridge cells fed by uni- and bidirectional DC/DC converters in (a) forward power flow condition and (b) reverse power flow condition.

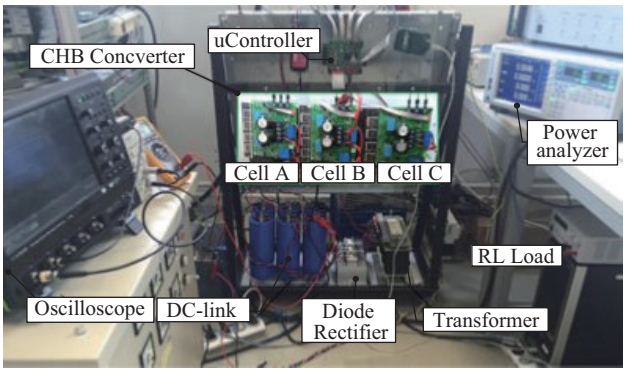

Fig. 15. Photograph of the experimental prototype.

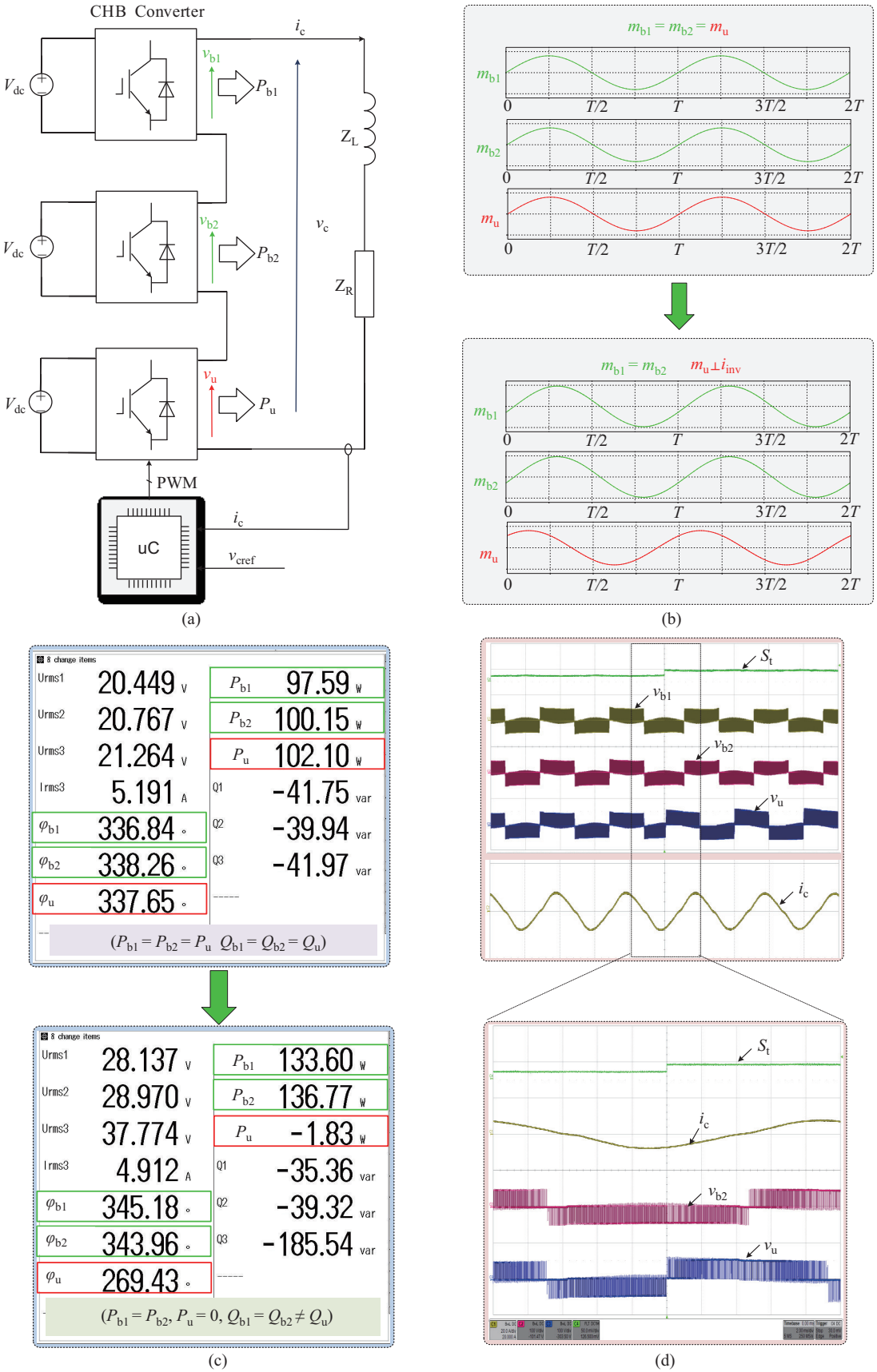

Fig. 16. The experimental procedure and experimental results. (a) Simplified structure schematic of the experimental prototype. (b) Modulation waveforms of three CHB cells in forward and reverse mode. (c) Output power of three CHB cells and the phase differences between the output current and the output voltages of three CHB cells. (d) The dynamic waveforms of output voltages and output current

In Fig. 15, the experimental prototype is controlled by the micro-controller, MPC5643L. The CHB converter is composed of IXYB82N120C3H1 IGBTs with 5 kHz switching frequency. The DC-link voltage of each cell $V_{\rm dc}$ is obtained through the diode rectifier and regulated to 50 V. The resistive and inductive loads, $Z_{\rm R} = 10.9\ \Omega$ and $Z_{\rm L} = 5.4\ \Omega$, are connected in series to the CHB converter.

In CHB grid-connected operation, the grid voltage is set as the oriented vector and the CHB output voltage reference $v_{\rm cref}$ is approximately close to the grid voltage. Here, it is set that the CHB output voltage reference $v_{\rm cref}$ is always with the constant amplitude 100 V and initial phase angle 0 rad, which is also set as the oriented vector. So, it is similar to the control of the CHB converter connected to the single-phase grid. The aim of the experiment is to validate the operation capability of the H-ST in the reverse power condition by the reactive power compensation and optimized distribution, thus the experiment is simplified as Fig. 16.

In forward mode, three cells (two bidirectional and one unidirectional cells) operate with the same modulation waveforms to generate the 100 V output voltage, and the modulation index $M_{\rm b1} = M_{\rm b2} = M_{\rm u} = 0.67$ as shown in Fig. 16(b). In this case, the output active power in each cell is almost the same ($P_{\rm b1} = 95.59$ W, $P_{\rm b2} = 100.15$ W, and $P_{\rm u} = 102.10$ W) as shown in Fig. 16(c). Besides, the power factor angles between output voltages in three cells and the inverter output current, ($\varphi_{\rm b1} = 336.85°$, $\varphi_{\rm b2} = 338.26°$, and $\varphi_{\rm u} = 337.68°$), are almost the same.

In order to verify the effect of reactive power compensation and optimized distribution in reverse mode, the third cell can not process the active power and the CHB output voltage $v_{\rm cref}$ still keeps the same as the previous condition to emulate the grid-connected scenario. In this case, if the unidirectional CHB cell deactivates, the bidirectional CHB cells would work with $M_{\rm b1} = M_{\rm b2} = 1$ according to the analysis in Section IV, which may cause over-modulation in grid-connected operation.

In this experiment, the reactive power compensation and optimized distribution are activated. The current angle is obtained through current PLL and the control system redistributes the modulation waveforms of the three cells. The modulation waveform of the unidirectional cell with $M_{\rm u} = 0.9$ is regulated to be orthogonal to the inverter output current $i_{\rm c}$, which can be seen $\varphi_{\rm u} = -\pi/2$ in Fig. 16(c). So the output active power of the third cell is near 0 W. The other two cells provide the left output voltage as analyzed in Section IV-B. In this case, the modulation index of two bidirectional CHB cells $M_{\rm b1} = M_{\rm b2}$ are reduced to 0.9, which enables the stable operation. The dynamic experimental waveforms of the converter output voltages and current are shown in Fig. 16(d). The waveforms of $S_{\rm t}$ is the trigger signal. When $S_{\rm t}$ steps increase, it can be seen that output PWM voltage of the third cell also has a step. The inverter current is almost not effected by the dynamic procedure, which is shown by the zoom-in waveforms in Fig. 16(d).

VI. Conclusion

In this paper the hybrid modular Smart Transformer, which combines the single active bridge-based series resonant converter (SAB-SRC) and dual active bridge (DAB) converter, is proposed. Based on the grid mission profile of asymmetrical power flow in both directions, the DAB converter-based modular Smart Transformer is not a cost-efficiency-benefit solution because the capacity of power semiconductors can not be fully used in reverse condition, while the hybrid modular Smart Transformer can avoid that drawback. Moreover, the unidirectional power module in the hybrid modular Smart Transformer can reduce 23.2% of cost and 35.3% of power losses compared with the bidirectional module in rated working condition, which increases the system efficiency in both the forward and reverse operation modes. The number of the SAB-SRC in the hybrid modular Smart Transformer is limited by the modulation index in the reverse mode. An improved control strategy, which is based on reactive power compensation control strategy, is presented to increase the SAB-SRC number. When a total of 13 cells are adopted, the operation region is extend by flexibly adjusting the unidirectional CHB cell modulation index. The simulation and experimental results both clearly validate the effectiveness of the theoretical analysis. However, in the reverse mode, the compensated reactive power is usually limited by the grid operation. So, the reactive power needs be further optimized by taking advantage of the proposed topology characteristics to reduce the compensated reactive power amount, which should be an emphasis in the future research.

Appendix A: Equations for Evaluation of The Performance

The equations used for evaluation of the performance are summarized as follows.

$$I_{\rm g} = \frac{2S_{\rm g}}{3V_{\rm g}} \tag{A1}$$

$$C_{\rm MV} \geq \frac{S_{\rm g}}{6n\omega V_{\rm MV}\Delta V} \tag{A2}$$

$$I_{\rm L(pk)} = \frac{V_{\rm MV}}{2\pi f_{\rm DAB} L_{\rm DAB}} \tag{A3}$$

$$I_{\rm L(RMS)} = I_{\rm L(pk)}\sqrt{1 - \frac{2\varphi}{3\pi}} \tag{A4}$$

$$I_{\rm M(RMS)} = I_{\rm L(pk)}\sqrt{\frac{1}{2} - \frac{\varphi}{3\pi}} \tag{A5}$$

$$N = \frac{V_{\rm winding}}{4A_{\rm c} f_{\rm DAB} B_{\rm pk}} \tag{A6}$$

$$A_{\rm w} = \frac{I_{\rm LRMS)}}{J} \tag{A7}$$

$$v_{\rm cu} = \frac{V_{\rm winding}}{4A_{\rm c} f_{\rm DAB} B_{\rm PK}} \cdot \frac{I_{\rm L(RMS)}}{J} l_{\rm mlp} \tag{A8}$$

$$W_{\rm cu} = v_{\rm cu} d_{\rm cu} \tag{A9}$$

$$C_{\rm cu} = K_{\rm c} W_{\rm cu} \tag{A10}$$

$$f_{\rm r} = \frac{1}{2\pi\sqrt{L_{\rm r} C_{\rm r}}},\ \omega_{\rm r} = 2\pi f_{\rm r} \tag{A11}$$

$$Z = \sqrt{\frac{L_{\rm r}}{C_{\rm r}}},\ \gamma = \pi\frac{f_{\rm r}}{f_{\rm s}}$$

$$I_{\rm i} = nI_{\rm o},\ I_{\rm o} = \frac{P_{\rm SRC}}{V_{\rm o}} \tag{A12}$$

$$I_{\mathrm{Lr(pk)}} = \frac{\pi}{2} n I_{\mathrm{o}} \quad V_{\mathrm{Cr(pk)}} = \frac{n I_{\mathrm{o}}}{4 f_s C_r} \tag{A13}$$

$$I_{\mathrm{s(rms)}} = I_{\mathrm{Lr(pk)}} \cdot \sqrt{\frac{1}{4} - \frac{1}{8\gamma}\sin(2\gamma)},\ I_{\mathrm{d(rms)}} = I_{\mathrm{s(rms)}} \tag{A14}$$

$$P_{\mathrm{I\_con}} = \frac{1}{T}\int_0^T v_{\mathrm{ce}}(i_{\mathrm{c}}, T_j, v_{\mathrm{g}}) \cdot i_{\mathrm{c}}(t)\mathrm{d}t \tag{A15}$$

$$P_{\mathrm{I\_con}} = v_{\mathrm{ce}} \cdot I_{\mathrm{c\_avg}} + R_{\mathrm{ce}} \cdot I^2_{\mathrm{c\_rms}} \tag{A16}$$

$$P_{\mathrm{I\_sw}} = \frac{1}{T}\Bigg(\sum_{n=1}^{N_{\mathrm{SW(on)}}} E_{\mathrm{on}}(v_{\mathrm{ce}}, i_{\mathrm{c}}, T_j, v_{\mathrm{g}}, R_{\mathrm{g}}) + \sum_{n=1}^{N_{\mathrm{SW(fff)}}} E_{\mathrm{off}}(v_{\mathrm{ce}}, i_{\mathrm{c}}, T_j, v_{\mathrm{g}}, R_{\mathrm{g}}) \Bigg) \tag{A17}$$

$$P_{\mathrm{D\_con}} = \frac{1}{T}\int_0^T (V_{\mathrm{D}} \cdot i_{\mathrm{D}} + R_{\mathrm{D}} \cdot i_{\mathrm{D}}^2)\mathrm{d}t \tag{A18}$$

$$P_{\mathrm{D\_con}} = V_{\mathrm{D}} \cdot I_{\mathrm{D\_avg}} + R_{\mathrm{D}} \cdot I^2_{\mathrm{D\_rms}} \tag{A19}$$

$$P_{\mathrm{D\_rr}} = \frac{1}{T}\int_0^T v_D \cdot i_{rr}\mathrm{d}t \tag{A20}$$

$$P_{\mathrm{M\_con}} = \frac{1}{T}\int_0^T v_{\mathrm{ds}}(i_{\mathrm{ds}}, T_j, v_{\mathrm{g}}) \cdot i_{\mathrm{ds}}(t)\mathrm{d}t \tag{A21}$$

$$P_{\mathrm{M\_con}} = R_{\mathrm{ds}} \cdot I^2_{\mathrm{ds}} \tag{A22}$$

$$P_{\mathrm{M\_sw}} = \frac{1}{T}\left(\sum_{n=1}^{N_{\mathrm{Sw(off)}}} E_{\mathrm{off}}(v_{\mathrm{ds}}, i_{\mathrm{d}}, T_j, v_{\mathrm{g}}, R_{\mathrm{g}}) \right) \tag{A23}$$

$$P_{\mathrm{wire}} = R_{\mathrm{wire}} \cdot I^2_{\mathrm{Tr(ms)}} \tag{A24}$$

$$P_{\mathrm{core}} = k_{\mathrm{v}} k_{\mathrm{i}} \lambda^{\beta-\alpha} (\mathrm{NA}_e)^{-\beta} \tag{A25}$$

$$k_{\mathrm{v}} = \frac{1}{T}\int_0^T |V(t)|^{\alpha}\mathrm{d}t \tag{A26}$$

$$P_{\mathrm{core}} = K_{\mathrm{stm}} f_{\mathrm{dc}}^{a_{\mathrm{stm}}} B_{\mathrm{pk}}^{\mathrm{b_{ptm}}} V_{\mathrm{core}} \tag{A27}$$

$$P_{\mathrm{d}} = \frac{1}{2} C V_{\mathrm{pP}} f \tan\delta \tag{A28}$$

$$P_{\mathrm{th}} = R_{\mathrm{e}} I^2_{\mathrm{cms}} \tag{A29}$$

REFERENCES

[1] M. Liserre, G. Buticchi, M. Andresen, G. De Carne, L. F. Costa, and Z. X. Zou, "The smart transformer: Impact on the electric grid and technology challenges," *IEEE Industrial Electronics Magazine*, vol. 10, no. 2, pp. 46–58, Jun. 2016.

[2] X. Liu, X. Liu, Y. Jiang, T. Zhang and B. Hao, "Photovoltaics and Energy Storage Integrated Flexible Direct Current Distribution Systems of Buildings: Definition, Technology Review, and Application," *CSEE Journal of Power and Energy Systems*, vol. 9, no. 3, pp. 829–845, May 2023.

[3] R. W. Zhu, G. Buticchi, and M. Liserre, "Investigation on common-mode voltage suppression in smart transformer-fed distributed hybrid grids," *IEEE Transactions on Power Electronics*, vol. 33, no. 10, pp. 8438–8448, Oct. 2018.

[4] X. Li and S. Wang, "Energy management and operational control methods for grid battery energy storage systems," *CSEE Journal of Power and Energy Systems*, vol. 7, no. 5, pp. 1026–1040, Sept. 2021,

[5] H. Mortazavi, H. Mehrjerdi, M. Saad, S. Lefebvre, D. Asber, and L. Lenoir, "A monitoring technique for reversed power flow detection with high pv penetration level," *IEEE Transactions on Smart Grid*, vol. 6, no. 5, pp. 2221–2232, Sep. 2015.

[6] A. K. Bhattacharjee, N. Kutkut, and I. Batarseh, "Review of multiport converters for solar and energy storage integration," *IEEE Transactions on Power Electronics*, vol. 34, no. 2, pp. 1431–1445, Feb. 2019.

[7] R. W. Zhu and M. Liserre, "Control of smart transformer under single-phase to ground fault condition,"*IEEE Transactions on Power Electronics*, vol. 35, no. 2, pp. 2034–2043, Feb. 2020.

[8] R. W. Zhu, G. De Carne, F. J. Deng, and M. Liserre, "Integration of large photovoltaic and wind system by means of smart transformer," *IEEE Transactions on Industrial Electronics*, vol. 64, no. 11, pp. 8928–8938, Nov. 2017.

[9] S. Pugliese, M. Andresen, R. A. Mastromauro, G. Buticchi, S. Stasi, and M. Liserre, "A new voltage balancing technique for a three-stage modular smart transformer interfacing a DC multibus," *IEEE Transactions on Power Electronics*, vol. 34, no. 3, pp. 2829–2840, Mar. 2019.

[10] X. She, A. Q. Huang, and R. Burgos, "Review of solid-state transformer technologies and their application in power distribution systems," *IEEE Journal of Emerging and Selected Topics in Power Electronics*, vol. 1, no. 3, pp. 186–198, Sep. 2013.

[11] G. Spiazzi and S. Buso, "Analysis of the interleaved isolated boost converter with coupled inductors," *IEEE Transactions on Industrial Electronics*, vol. 62, no. 7, pp. 4481–4491, Jul. 2015.

[12] H. F. Fan and H. Li, "High-frequency transformer isolated bidirectional DC-DC converter modules with high efficiency over wide load range for 20 kva solid-state transformer," *IEEE Transactions on Power Electronics*, vol. 26, no. 12, pp. 3599–3608, Dec. 2011.

[13] H. S. Qin and J. W. Kimball, "Solid-state transformer architecture using AC-AC dual-active-bridge converter," *IEEE Transactions on Industrial Electronics*, vol. 60, no. 9, pp. 3720–3730, Sep. 2013.

[14] J. J. Yao, W. Chen, C. Y. Xue, Y. B. Yuan, and T. Wang, "An ISOP hybrid DC transformer combining multiple SRCs and DAB converters to interconnect MVDC and LVDC distribution networks," *IEEE Transactions on Power Electronics*, vol. 35, no. 11, pp. 11442–11452, Nov. 2020.

[15] T. B. Soeiro and J. W. Kolar, "Analysis of high-efficiency three-phase two- and three-level unidirectional hybrid rectifiers," *IEEE Transactions on Industrial Electronics*, vol. 60, no. 9, pp. 3589–3601, Sep. 2013.

[16] L. Wang, D. L. Zhang, Y. Wang, B. Wu, and H. S. Athab, "Power and voltage balance control of a novel three-phase solid-state transformer using multilevel cascaded h-bridge inverters for microgrid applications," *IEEE Transactions on Power Electronics*, vol. 31, no. 4, pp. 3289–3301, Apr. 2016.

[17] M. Coppola, F. Di Napoli, P. Guerriero, D. Iannuzzi, S. Daliento, and A. Del Pizzo, "An FPGA-based advanced control strategy of a GridTied PV CHB inverter," *IEEE Transactions on Power Electronics*, vol. 31, no. 1, pp. 806–816, Jan. 2016.

[18] M. Moosavi, G. Farivar, H. Iman-Eini, and S. M. Shekarabi, "A voltage balancing strategy with extended operating region for cascaded h-bridge converters," *IEEE Transactions on Power Electronics*, vol. 29, no. 9, pp. 5044–5053, Sep. 2014.

[19] W. Mao, X. Zhang, T. Zhao, Y. H. Hu, F. S. Wang, Z. Q. Dai, and R. X. Cao, "Research on power equalization of three-phase cascaded h-bridge photovoltaic inverter based on the combination of hybrid modulation strategy and zero-sequence injection methods," *IEEE Transactions on Industrial Electronics*, vol. 67, no. 11, pp. 9337–9347, Nov. 2020.

[20] L. M. Liu, H. Li, Y. S. Xue, and W. X. Liu, "Decoupled active and reactive power control for large-scale grid-connected photovoltaic systems using cascaded modular multilevel converters," *IEEE Transactions on Power Electronics*, vol. 30, no. 1, pp. 176–187, Jan. 2015.

[21] L. F. Costa, G. Buticchi, and M. Liserre, "A family of series-resonant DC-DC converter with fault-tolerance capability," *IEEE Transactions on Industry Applications*, vol. 54, no. 1, pp. 335–344, Jan./Feb. 2018.

[22] L. F. Costa, G. Buticchi, and M. Liserre, "Highly efficient and reliable SiC-based DC-DC converter for smart transformer," *IEEE Transactions on Industrial Electronics*, vol. 64, no. 10, pp. 8383–8392, Oct. 2017.

[23] D. Wang, J. Tian, C. X. Mao, J. M. Lu, Y. P. Duan, J. Qiu, and H. H. Cai, "A 10-kV/400-V 500-kVA electronic power transformer," *IEEE Transactions on Industrial Electronics*, vol. 63, no. 11, pp. 6653–6663, Nov. 2016.

[24] Y. C. Jeung and D. C. Lee, "Voltage and current regulations of bidirectional isolated dual-active-bridge DC-DC converters based on a double-integral sliding mode control," *IEEE Transactions on Power Electronics*, vol. 34, no. 7, pp. 6937–6946, Jul. 2019.

[25] U. Drofenik and J. W. Kolar, "Thermal power density barriers of converter systems," in *Proceedings of 5th International Conference on Integrated Power Electronics Systems*, 2008, pp. 1–5.

[26] L. F. Costa, F. Hoffmann, G. Buticchi, and M. Liserre, "Comparative analysis of multiple active bridge converters configurations in modular smart transformer," *IEEE Transactions on Industrial Electronics*, vol. 66, no. 1, pp. 191–202, Jan. 2019.

[27] K. Wang, M. Andresen, Y. Ko, and M. Liserre, "Cascaded multilevel topology based on quadruple active bridges for phase power balancing in large-scale PV systems," in *Proceedings of 2019 21st European Conference on Power Electronics and Applications (EPE'19 ECCE Europe)*, 2019, pp. P.1-P.8.
[28] M. K. Kazimierczuk, High-Frequency Magnetic Components. Hoboken: John Wiley & Sons, 2009.
[29] R. W. Zhu, F. Hoffmann, N. Vázquez, K. G. Wang, and M. Liserre, "Asymmetrical bidirectional DC-DC converter with limited reverse power rating in smart transformer," *IEEE Transactions on Power Electronics*, vol. 35, no. 7, pp. 6895–6905, Jul. 2020.
[30] H. Akagi, S. Inoue, and T. Yoshii, "Control and performance of a transformerless cascade pwm statcom with star configuration," *IEEE Transactions on Industry Applications*, vol. 43, no. 4, pp. 1041–1049, Jul./Nov. 2007.
[31] K. Wang, M. Andresen, S. Pugliese, and M. Liserre, "Phase power balancing of interphase grid-connected CHB-QAB PV systems," in *Proceedings of 44th Annual Conference of the IEEE Industrial Electronics Society*, 2018, pp. 3363–3368.

Kangan Wang received B.S. and Ph.D. degrees in Electrical Engineering from China University of Mining and Technology, Xuzhou, China, in 2013 and 2019, respectively. From 2017 to 2019, He was a Visiting Ph.D. Student with the Chair of Power Electronics, Department of Electrical and Electronic Engineering, Christian-Albrechts University of Kiel, Kiel, Germany. Since 2020, he has been with Logistics Engineering College, Shanghai Maritime University. His research interests include power electronic-based smart transformer, multilevel converters and high-power DC/DC converters with isolation.

Youngjong Ko received B.S. and M.S. degrees in Electronic Engineering from Ajou University, Suwon, South Korea, in 2009 and 2012, respectively, and the Ph.D. degree from the Chair of Power Electronics, Christian-Albrechts University of Kiel, Kiel, Germany, in 2019. He was a Researcher with LG Chem, Daejeon, South Korea, from 2019 to 2020. Since 2020, he has been an Assistant Professor and holding Power Electronics Application Laboratory, Department of Electrical Engineering and Industry 4.0 Convergence Bionics Engineering, Pukyong National University, Busan, South Korea. His current research interests include the control and modulation of power converters, and reliability in power electronics.

Rongwu Zhu received the B.Eng. degree in Electrical Engineering from Nanjing Normal University, Nanjing, China, in 2007, and the Ph.D. degree in Energy Technology from the Department of Energy Technology, Aalborg University, Aalborg, Denmark, in 2015. From 2011 to 2012, he was a Guest Researcher with Aalborg University. From 2016 to 2021, he was a Senior Researcher with the Chair of Power Electronics, Christian-Albrechts University of Kiel, Kiel, Germany. He is currently a Full Professor and the Director of Department of Electrical Engineering, Harbin Institute of Technology, Shenzhen, China. He is also the Director of the joint lab of modern distribution power system and intelligent equipment. He has authored and coauthored around 130 technical papers (more than 1/3 of them in international peer-reviewed journals/magazine), 1 book chapter and 20 granted or pending patents. His research interests include renewables integration, control, operation and digitalization of power electronics, and renewables-dominated grid. He served as Editor of the International Transactions on Electrical Energy System, Associate Editor for Renewable Power Generation, Associate Editor for IEEE Open Journal of Power Electronics, and Guest Associate Editor for the IEEE Journal of Emerging and Selected Topics in Power Electronics, Guest Editor-in-Chief of CSEE Journal of Power and Energy Systems, and Committee Chairperson for several International Conferences.

Siyu Wu received B.E. and M.S. degrees in Electrical Engineering from Shanghai Maritime University, Shanghai, China, in 2021 and 2023, respectively. Currently, he is a researcher with Sungrow Power Supply Co., Ltd in Shanghai, China. His research interests include the improved topology architectures and advanced control strategies of power electronics transformers, focusing on the high-power DC-DC converters with isolation.

Weimin Wu received Ph.D. degree in Electrical Engineering from the College of Electrical Engineering, Zhejiang University, Hangzhou, China, in 2005. He worked as a Research Engineer in the Delta Power Electronic Centre (DPEC), Shanghai, from July, 2005 to June, 2006. From 2006 to 2023, he was with Department of Electrical Engineering, Shanghai Maritime University. He joined Anhui University of Science and Technology in 2024. Currently, he is the Dean of the School of Electrical and Information Engineering, Anhui University of Science and Technology. He was a Visiting Professor in the Centre for Power Electronics Systems (CPES), Virginia Polytechnic Institute and State University, Blacksburg, USA, from September 2008 to March 2009. From November 2011 to January 2014, he was also a Visiting Professor with the Department of Energy Technology, Aalborg University, Aalborg, Demark, working with the Centre of Reliable Power Electronics. He has coauthored more than 200 papers and holds 8 patents. His research interests include power converters for renewable energy systems, power quality, smart grid, and energy storage technology.

Marco Liserre received M.Sc. and Ph.D. degrees in Electrical Engineering from the Bari Polytechnic in 1998 and 2002, respectively. He has held the position of Associate Professor at Bari Polytechnic and since 2012, he has been a Professor of Reliable Power Electronics at Aalborg University in Denmark. In 2013, he became a Full Professor and assumed the role of Chair of Power Electronics at Kiel University in Germany. He has published 500 technical papers, with one-third appearing in international peer-reviewed journals, and authored a book. His works have garnered over 35,000 citations. Marco Liserre has been included in the ISI Thomson report "The world's most influential scientific minds" since 2014. He has received an ERC Consolidator Grant for his project titled "The Highly Efficient and Reliable smart Transformer (HEART), a new Heart for the Electric Distribution System." He is a member of IAS, PELS, PES, and IES, where he has served in various capacities. He has been honored with numerous awards, including the IES 2009 Early Career Award, the IES 2011 Anthony J. Hornfeck Service Award, the 2014 Dr. Bimal Bose Energy Systems Award, the Industrial Electronics Magazine Best Paper Award in 2011 and 2020, the Third Prize Paper Award by the Industrial Power Converter Committee at ECCE 2012, the 2017 IEEE PELS Sustainable Energy Systems Technical Achievement Award, and the 2018 IEEE-IES Mittelmann Achievement Award.